JOURNAL OF COMPUTATIONAL PHYSICS **123,** 450–465 (1996)
ARTICLE NO. 0036

Numerical Simulation of a Cylinder in Uniform Flow: Application of a Virtual Boundary Method

E. M. SAIKI AND S. BIRINGEN

Department of Aerospace Engineering Sciences, University of Colorado, Boulder, Colorado

Received July 12, 1994; revised July 10, 1995

In this study, a virtual boundary technique is applied to the numerical simulation of stationary and moving cylinders in uniform flow. This approach readily allows the imposition of a no-slip boundary within the flow field by a feedback forcing term added to the momentum equations. In the present work, this technique is used with a high-order finite difference method, effectively eliminating spurious oscillations caused by the feedback forcing when used with spectrally discretized flow solvers. Very good agreement is found between the present calculations and previous computational and experimental results for steady and time-dependent flow at low Reynolds numbers.

INTRODUCTION

The fundamental fluid dynamics problem of a circular cylinder in uniform flow has been examined extensively in both computational and experimental studies and is considered a stringent test for flow solvers. The difficulty which accompanies the computational approach to this problem by finite differences or spectral methods lies in the representation of the cylinder geometry to allow for an accurate application of these numerical integration methods. The use of coordinate transformations and mapping techniques is possible but requires a highly accurate way of calculating the transformation Jacobians. Finite element methods (Gresho *et al.*[17]; Engelman and Jaminia [11]; Karniadakis and Triantafyllou [21]) and conformal transformations (Jordan and Fromm [20]; Braza *et al.* [4]; Badr and Dennis [1]) have been successfully used for this problem. As an alternative to the use of generalized coordinates and coordinate transformations for finite difference and spectral methods, Peskin [23] developed a method which represents a body within a flow field via a forcing term added to the governing equations. When applied at certain points in the flow, this forcing term simulates the effect of the body on the flow, allowing for the modeling of a boundary of any shape within a Cartesian computational box without the necessity of mapping. Peskin [23, 24] successfully implemented this method (immersed boundary technique) to model moving boundaries in heart valve simulations. The main advantage of the scheme lies in its ability to model the material properties of the body and movement of the boundaries. However, numerical stiffness of most moving boundary problems restricts the explicit definition of the forcing term in Peskin's method to small time steps (Tu and Peskin [32]). This method has been expanded and implemented in a number of other problems modeling suspended particulates (Fogelson and Peskin [12]) and the inner ear (Beyer [3]).

In a related, yet independent, study, Goldstein *et al.* [15, 16] developed a virtual boundary method based on the initial work of Sirovich [28, 29] which employs a forcing term governed by a feedback loop. Using a spectral method, they applied this procedure to investigate the effects of riblets on turbulent channel flow and to flow between concentric cylinders. They noted that the forcing function generated constant low amplitude, high frequency oscillations which they were able to control by numerical low-pass filters and/or the introduction of particular flow fields inside of the body. Their simulations were not noticeably affected by these spurious signals, but such numerical oscillations may become of concern when one calculates the evolution of a forced disturbance wave as in the simulation of flow instability and transition.

In the present study, we use the method developed by Goldstein *et al.* [16] to simulate stationary, rotating, and oscillating cylinders in uniform flow at low Reynolds numbers ($Re \leq 400$) allowing the assessment of the virtual boundary technique to model a body in an unsteady flow field. In the present solution procedure, high-order finite differences are implemented in order to suppress the numerical oscillations caused by the forcing function observed in the Chebyshev spectral method of Goldstein *et al.* [16].

COMPUTATIONAL METHOD

The numerical model integrates the two-dimensional, time-dependent, incompressible, Navier-Stokes, and continuity equations nondimensionalized by the diameter of the cylinder, D, and the free-stream velocity, U_∞, on a staggered mesh by a time-splitting method. The normal

0021-9991/96 $18.00

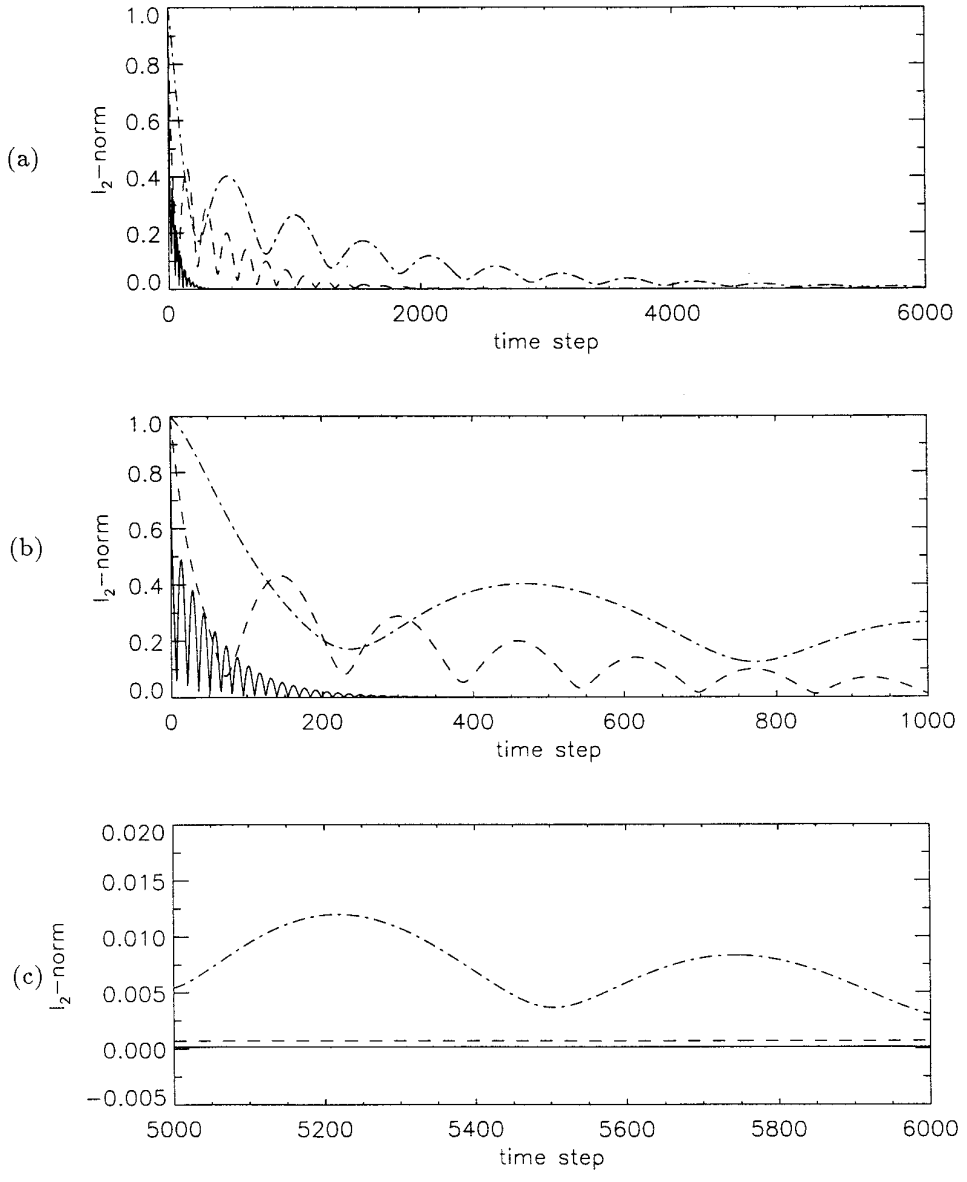

FIG. 1. Time distribution of the l_2-norm error in the no-slip condition imposed by the virtual boundary method defining a cylinder in uniform flow at Re = 25. Comparison between solutions with varying α/β: (a) over total run time; (b) closeup of first 1000 time steps; and (c) closeup of last 1000 time steps. $\alpha = -400000$, $\beta = -600$, ———; $\alpha = -4000$, $\beta = -60$, – – –; $\alpha = -400$, $\beta = -6$, --------.

diffusion terms are advanced implicitly by the Crank–Nicolson scheme and either the explicit third-order compact Runge–Kutta or Adams–Bashforth methods are applied to the remaining terms (Streett and Hussaini [30]). The equations are discretized spatially in the normal (y) and streamwise (x) directions by fourth-order central finite differences. The pressure Poisson equation is evaluated by the tensor product method (Huser and Biringen [19]).

At the upper and lower boundaries, we impose shear free conditions, i.e., $\partial u/\partial y = 0$ and $v = 0$ and at the inflow boundary, uniform flow conditions are assumed, *i.e.*, $u = 1$ and $v = 0$. At the outflow, boundary conditions are prescribed to ensure that wave-like disturbances (generated by vortex shedding) in the high Reynolds number cases leave the computational domain without reflection. This was accomplished by appending a "buffer domain" to the physical domain (the length of the buffer domain was about 20–30% of the physical domain) in which the governing equations were modified by reducing the streamwise viscous terms and the right-hand side of the pressure Poisson equation to zero at the outflow boundary using a

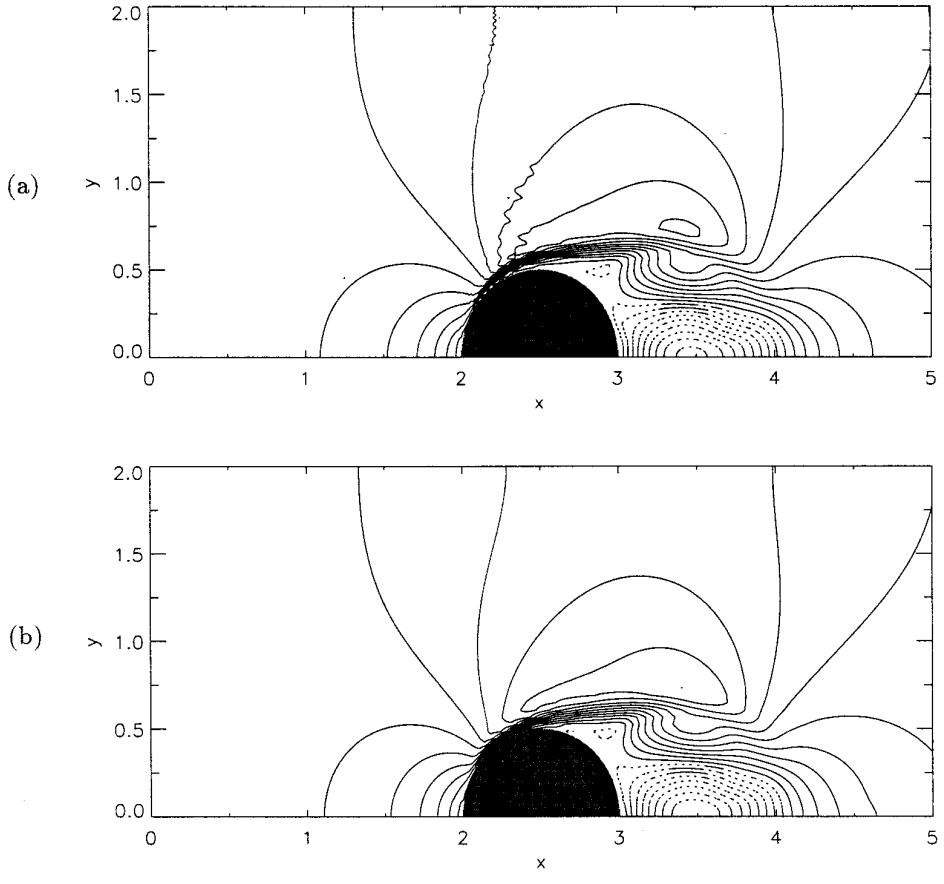

FIG. 2. Re = 550, $t = 3$: streamwise velocity. (a) Chebyshev; (b) finite differences.

smooth coefficient function. Previous numerical experiments have included rigorous testing of this technique, verifying its suitability for use in both high and low amplitude wave propagation problems (Streett and Macaraeg [31]; Danabasoglu [9]; Danabasoglu *et al.* [10]; Saiki *et al.* [26]).

In implementing the method of Goldstein *et al.* [16] to the present calculations of flow over a cylinder, the no-slip boundary of the cylinder surface was represented by a feedback forcing function added to the momentum equations. This feedback function effectively brings the fluid velocity to zero at the desired points in the flow which define the no-slip boundary and can be expressed as

$$\mathbf{F}(\mathbf{x}_s, t) = \alpha \int_0^t (\mathbf{U}(\mathbf{x}_s, t) - \mathbf{v}(\mathbf{x}_s, t))\, dt + \beta(\mathbf{U}(\mathbf{x}_s, t) - \mathbf{v}(\mathbf{x}_s, t)). \quad (1)$$

Here, $\mathbf{F}$ is the external force imposed at the discrete surface points defined by $\mathbf{x}_s$, and $\mathbf{U}$ is the fluid velocity at these surface points. The velocity of the body itself is controlled by specifying $\mathbf{v} = (u_b, v_b)$ at the boundary points. If the body moves, i.e., $\mathbf{v} \neq 0$, then the position of the boundary points at each time step is computed by integration of $\mathbf{v} = d\mathbf{x}_s/dt$. The negative constants α and β are determined by observing the response of $\mathbf{U}$ once $\mathbf{F}$ is applied; α produces the natural oscillation frequency of the response, while β dampens the oscillation of the response. For unsteady flows, α must produce a response with a natural frequency greater than the highest frequencies present in the flow so that $\mathbf{F}$ can respond correctly to the changing flow field. The oscillatory nature of the boundary does not affect the overall steady state of the flow field. However, for each combination of α and β a different forcing function is added to the right-hand side of the momentum equations, therefore a set of similar but slightly different flow fields are obtained for each of the solutions. For example, comparison of the cylinder cases presented below revealed variations of 1–2% in the geometrical parameters of the wake.

To examine the response of the virtual boundary to different α/β combinations, a stationary cylinder at Re = 25 was modeled and the l_2-norm error of the velocities at the boundary points with respect to the no-slip boundary

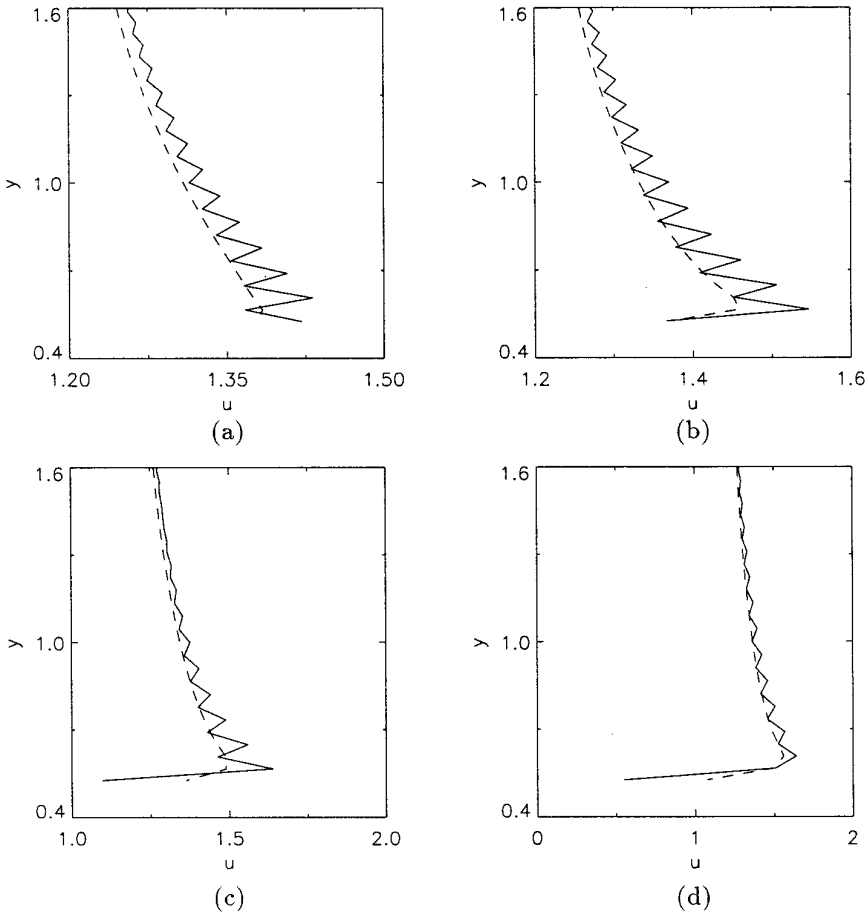

FIG. 3. Re = 550: normal profiles of streamwise velocity in the vicinity of the cylinder. (a) $x = 2.23750$; (b) $x = 2.2875$; (c) $x = 2.3125$; (d) $x = 2.3650$. Chebyshev, ———; finite differences – – –.

condition was tracked in time. The l_2-norm in the streamwise velocity is defined as

$$l_2\text{-norm} = \sqrt{\frac{1}{n_b}\sum_{i=1}^{n_b}(u_b)_i^2}, \tag{2}$$

where n_b is the number of virtual boundary points. The results of this analysis are presented in Fig. 1. With the application of the higher values of these parameters, the no-slip boundary condition is quickly attained. At the end of the time period considered, the l_2-norm corresponding to the lower α/β values is two orders of magnitude higher than the other two cases; however, it continues to decay. These test cases suggest that higher values of the coefficients allow the method to respond faster to any unsteadiness in the flow field and act more efficiently in reinforcing the no-slip conditions. These computations were conducted using $n_b = 1441$ boundary points; further increases or decreases in n_b with the same values of α and β yielded similar results.

The time step restricting this method is based upon the values of α and β and the explicit time integration implemented in the flow solver. For the Adams–Bashforth method, Goldstein *et al.* [16] determined the following expression for the time step

$$\Delta t < \frac{-\beta - \sqrt{(\beta^2 - 2\alpha k)}}{\alpha}, \tag{3}$$

where k is a problem dependent constant of order one. A similar restriction was observed in the current study when the Runge–Kutta method was used.

In order to represent the body boundary in the flow field, Goldstein *et al.* [16] defined the boundary on points which coincided with the computational grid nodes, whereas Peskin [23, 24] and Goldstein *et al.* [15] defined the body boundary in a manner independent of the computational grid. Peskin [23] utilized a first-order cosine function to interpolate and extrapolate information between the immersed boundary and the grid. More

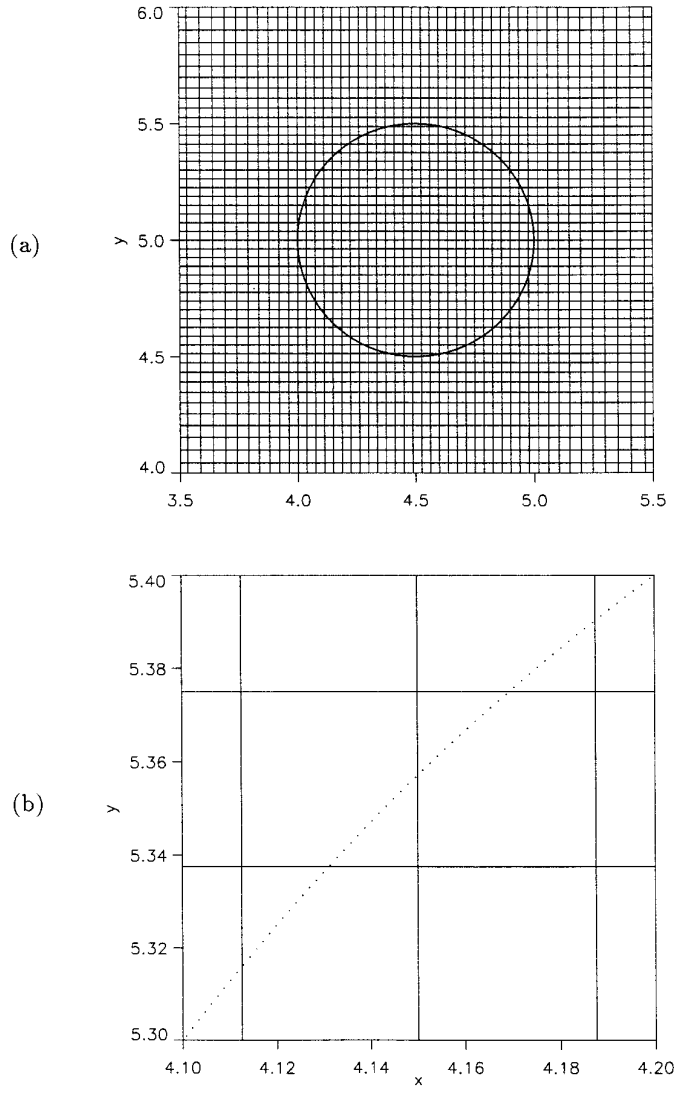

FIG. 4. Superposition of the virtual boundary points on the computational grid: (a) full cylinder body; (b) upper left portion of the cylinder.

recently, Beyer [3] developed a second-order accurate representation of the immersed boundary in applications of Peskin's method. Goldstein *et al.* [15] implemented highly accurate spectral interpolation of the velocities from the grid points to the virtual boundary points and applied linear interpolation to distribute the effect of the forcing term to the grid nodes.

In the current study, the fluid velocities are interpolated to a virtual boundary point, (x_s, y_s), from the four surrounding grid points denoted by the indices (i, j), $(i+1, j)$, $(i, j+1)$, and $(i+1, j+1)$, using bilinear interpolation,

$$\mathbf{U}(\mathbf{x}_s) = \sum_{i,j}^{i+1,j+1} D_{i,j}(\mathbf{x}_s)\mathbf{U}_{i,j}, \tag{4}$$

where

$$D_{i,j}(\mathbf{x}_s) = d(x_s - x_i)d(y_s - y_j). \tag{5}$$

In Eq. (5),

$$d(x_s - x_i) = \frac{(x_s - x_{i+1})}{(x_i - x_{i+1})} \quad \text{if } x_i < x_s \tag{6a}$$

$$d(x_s - x_i) = \frac{(x_s - x_{i-1})}{(x_i - x_{i-1})} \quad \text{if } x_i > x_s \tag{6b}$$

and

$$d(x_s - x_i) = 1 \quad \text{if } x_i = x_s. \tag{6c}$$

The effect of the virtual boundary force is extrapolated back to the grid points by area-weighted averages,

$$\mathbf{F}_{i,j} = \frac{1}{N_b} \sum_{n=1}^{N_b} D_{i,j}(\mathbf{x}_s)\mathbf{F}_n(\mathbf{x}_s), \tag{7}$$

where N_b is the number of virtual boundary points which affect the (i, j)th grid point. This method of spreading the boundary forces results in an effective boundary thickness on the order of one grid cell, i.e., $O(\Delta x, \delta y)$. The above interpolation/extrapolation scheme is first-order accurate, similar to the delta function representation of Peskin [23]. The low order accuracy of this operation influences mainly the flow field in the immediate vicinity of the cylinder; however, large scale features are successfully captured by this method.

Both Peskin [23, 24] and Goldstein *et al.* [15, 16] imposed the forcing term only at points which defined the boundary, thus allowing fluid motion inside the body. For Peskin's [23, 24] work this behavior is desirable since his calculations concern blood flow inside of the heart and the external flow field is ignored. Goldstein *et al.* [15, 16] investigated the effect of solid bodies placed within a flow field which physically do not permit flow inside the boundary. Consequently, the flow fields which were numerically allowed to develop in such boundaries were unphysical; however, the internal flow field was used as a smoothing device to attenuate spatial oscillations generated by the method (Goldstein *et al.* [15, 16]). In the present computations, some of the test cases (in particular, the Re = 550 case presented below) converged to an incorrect solution with the forcing term imposed only on the boundary. This behavior was remedied by imposing the forcing function *inside* the boundary of the body, as well as on the boundary. This suggests that in implementing the virtual boundary technique in solid body problems, where the solution is unknown, the forcing

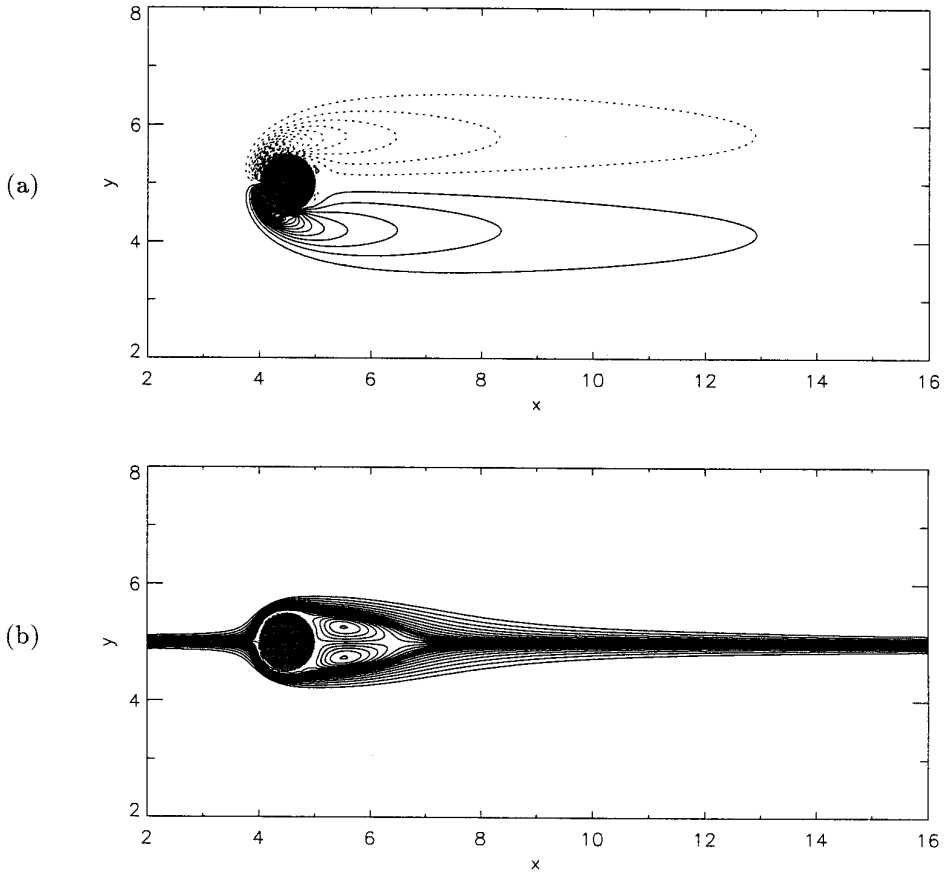

FIG. 5. Re = 25: (a) spanwise vorticity, dotted and solid lines denote negative and positive levels, respectively; (b) streamfunction.

term should be applied at the boundary and interior points of the body in order to converge to a correct solution.

In an earlier work by the authors [27], the virtual boundary technique was used with a different flow solver implementing Chebyshev polynomials in the wall-normal direction. Due to the global nature of the Chebyshev polynomials, nongrowing, spatial oscillations in the normal and streamwise directions developed in the flow field when the feedback forcing function was applied. The virtual boundary acts as a discontinuity in the spectral representation of the flow field, thus causing the oscillations to arise (Gibb's phenomenon). These oscillations were similar to those also observed by Goldstein *et al.* [16] and did not appear to affect the flow field downstream of the body. In the present work, the application of a local discretization scheme, i.e., finite differences, in the normal direction drastically reduced the amplitude of these spatial oscillations. The effect of these different discretization methods (i.e., the Chebyshev and finite difference methods) is illustrated in results obtained from computations of startup flow over a cylinder at Re = 550 (Figs. 2 and 3). Contours of streamwise velocity reveal the spatial oscillations which arise due to the Chebyshev discretization (Fig. 2a), and Fig. 2b shows the attenuation of the oscillations with the application of finite differences. Comparison of the streamwise profiles in the normal direction (Fig. 3) provide clear evidence that the oscillations are strongly damped.

RESULTS

Stationary Cylinder in Uniform Flow

The cases investigating uniform flow over a stationary cylinder examined Reynolds numbers ($\mathrm{Re} = U_\infty D/\nu$) ranging from Re = 25 to Re = 400. The mesh resolution varied from 267×147 to 436×147 for computational domains ranging from 20×10 to 34×10. As the Reynolds number increased, the length of the computational domain was increased in order to accommodate the stronger vortices which were shed from the cylinder. These adjustments are reflected in the varying grid and domain sizes cited above. Mesh stretching was employed in both directions with grid clustering near the body: the minimum grid spacing in the vicinity of the cylinder for all cases was $\Delta x_{\min} = \Delta y_{\min} = 0.0375$. The feedback forcing coefficients were set to $\alpha = -400000$ and $\beta = -600$, and the number of points defining the cylinder was 1441. The distribution of points defining

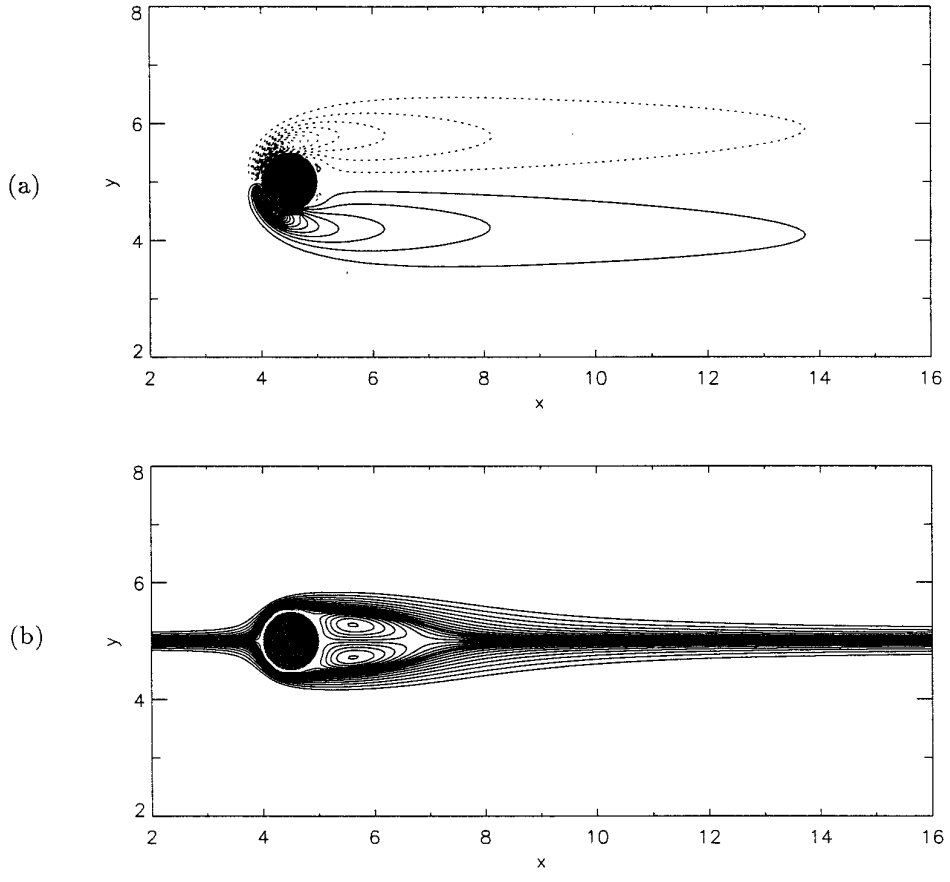

FIG. 6. Re = 30 : (a) spanwise vorticity, dotted and solid lines denote negative and positive levels, respectively; (b) streamfunction.

TABLE I

Comparison of the Wake Properties behind a Stationary Cylinder with Experiments and Previous Computational Results for Re = 25 and Re = 30; Steady Flow Solutions

	Re = 25				Re = 30		
Properties of the wake behind a stationary cylinder	Present results	Gresho *et al.* [17][a]	Coutanceau & Bouard [6][b]	Clift *et al.* [5][b]	Present results	Coutanceau & Bouard [6][b]	Clift *et al.* [5][b]
Length of the separation bubble (L)	1.41	1.15	1.22	—	1.7	1.53	—
x-coordinate of the center of the vortex cores (a)	0.53	0.38	0.44	—	0.62	0.55	—
y-distance between the vortex cores (b)	0.5	0.47	0.51	—	0.5625	0.54	—
Minimum streamwise velocity on the axis of symmetry (u_{max})	−0.064	−0.057	−0.057	—	−0.08	−0.0743	—
x-coordinate of minimum streamwise velocity on the axis of symmetry (d)	0.59	0.49	0.5	—	0.72	0.64	—
Separation angle (θ)	45°	45°	48°	—	48°	50.1°	—
Drag coefficient (C_d)	1.54	2.26	—	1.84	1.38	—	1.69

[a] Computational study.
[b] Experiment.

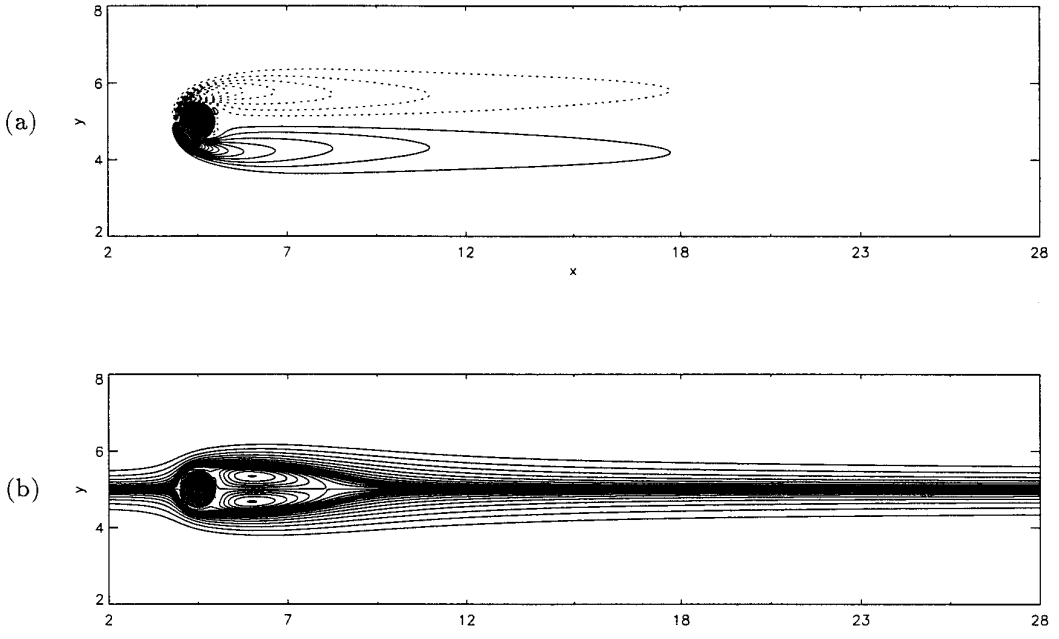

FIG. 7. Re = 50 : steady state solution. (a) spanwise vorticity, dotted and solid lines denote negative and positive levels, respectively; (b) stream-function.

the virtual boundary superimposed onto the computational grid is presented in Fig. 4. In this particular case, we chose to impose the virtual boundary only on points defining the boundary of the cylinder; similar results were obtained when points were imposed in the interior. The velocity components of the boundary points, **v**, were set to zero.

At low Reynolds numbers, ($4.5 \leq \mathrm{Re} \leq 35$), experiments reveal an attached, steady, symmetric, recirculating bubble which develops downstream of the cylinder (Coutanceau and Defaye [7]). In the present simulations this behavior is clearly observed in the stream-function and spanwise vorticity contours for Re = 25 and Re = 30, respectively

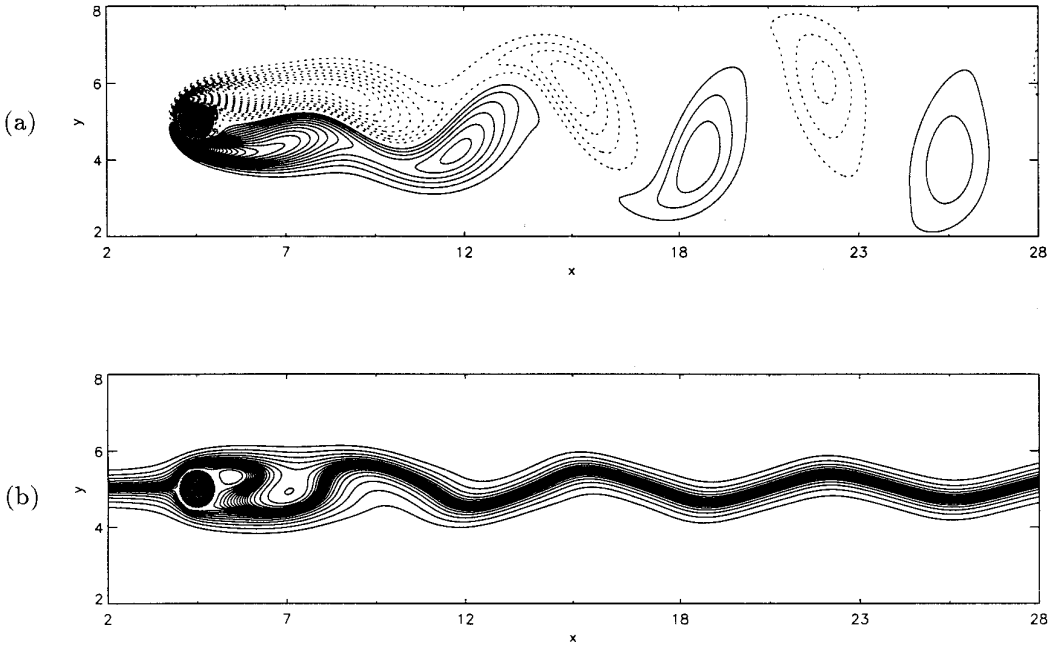

FIG. 8. Re = 50 : unsteady solution. (a) spanwise voriticity, dotted and solid lines denote negative and positive levels, respectively; (b) stream-function.

TABLE II

Comparison of Quantitative Data with Results from Experiments and Previous Computational Studies; Unsteady Flow Solutions

	Drag coefficient: C_d[a]			Strouhal number: St				Wavelength: λ		Vortex speed: St λ	
Re	Present results	Gresho *et al.* [17][b]	Clift *et al.* [5][c]	Present results	Gresho *et al.* [17][b]	Roshko [26][c]	Berger & Wille [2][c]	Present results	Gresho *et al.* [17][b]	Present results	Gresho *et al.* [17][b]
50[d]	1.38	1.81	1.41	0.139	0.14	0.122	0.12–0.13	6.9	6.5	0.96	0.93
65	1.33	—	1.33	0.152	—	0.143	—	6.3	—	0.96	—
100	1.26	1.76	1.24	0.171	0.18	0.167	0.16–0.17	5.5	5.2	0.94	0.93
200	1.18	1.76	1.16	0.197	0.21	—	0.18–0.19	4.7	4.4	0.93	0.92
400	1.18	1.78	1.12	0.22	0.22	0.205	0.2–0.21	4.2	4.4	0.92	0.96

[a] Drag coefficient is averaged in the unsteady cases.
[b] Computational study.
[c] Experiment.
[d] Unsteady solution (Fig. 7).

(Figs. 5 and 6). The physical parameters of the separation bubble are compared with previous experimental and computational studies in Table I and show good agreement for both Reynolds numbers.

When the Reynolds number is increased to values in the $35 \leq \mathrm{Re} \leq 60$ range, experiments observe asymmetry of the separation bubble and ''wavy'' behavior of the tail of the wake. In the current computations it was found that for Reynolds numbers in this range (in particular, Re = 50) the type of wake behavior depends on whether the initial conditions are perturbed. For example, if no forced perturbations are imposed a steady separation bubble develops downstream of the cylinder (Fig. 7). The length of the separation bubble in this case is $L = 3$ in agreement with the steady state computation of Fornberg [13] at Re = 50. If the solution shown in Fig. 7 is disturbed by introducing a small perturbation in the flow field, vortex shedding is instigated. This behavior is demonstrated in Fig. 8, where the cylinder was moved vertically 0.001 nondimensional units away from its original position and then moved back, perturbing the flow field and generating a Kármán vortex street. At Re = 50, Gresho *et al.* [17] also observed vortex shedding from the cylinder with no attached separation bubble, and the wake characteristics measured in the unsteady solution of the current study show good agreement compared with Gresho *et al.*'s [17] results (Table II). In the computational studies of Jordan and Fromm [20] and Braza *et al.* [4], no vortex shedding or asymmetry of the separation bubble was observed for Reynolds numbers up to 1000. Braza *et al.* [4] explained this behavior by stating that the computational scheme was too ''clean,'' i.e., no external perturbations existed (as would appear in an experiment), therefore there was nothing to trigger any asymmetry or unsteadiness of the flow field. To induce the vortex shedding in their simulations, the flow field was numerically perturbed. Similarly, in the present study a perturbation was needed in order to obtain vortex shedding at Re = 50; however, the higher Reynolds number cases did not require any external perturbations. Consequently, Re = 50 is close to a critical Reynolds number above which the solution becomes unsteady. It is possible that the steady state solution obtained for Re = 50 may eventually exhibit unsteadiness due to the buildup of truncation and machine errors in the solution, but the computer time needed to arrive at this point would be considerable.

According to experimental results, increasing the Reynolds number beyond Re = 60 leads to the development of a Kármán vortex street forced by vortices which are shed alternately with a distinct frequency from the top and bottom of the cylinder (Coutanceau and Defaye [7]). In the present study, the formation of the vortex street is depicted clearly in spanwise vorticity contours for Re = 65, 100, 200, and 400 (Fig. 9). In Fig. 10, vertical velocity contours for Re = 400 are plotted, indicating a very smooth solution that is free of any detectable residual oscillations. As the Reynolds number increases, the frequency of the shedding increases (Table II) and the vortices become more concentrated. The patterns obtained for Re = 65 and Re = 100 show remarkable similarity to the flow visualizations of Freymuth *et al.* [14]. The time spectra and signature of the streamwise velocity at a point downstream of the cylinder reveals the presence of a spike at the vortex street Strouhal number ($\mathrm{St} = U_\infty f/D$: f = dimensional frequency); higher harmonics of the Strouhal number are also present (Fig. 11). Experiments predict that the onset of three-dimensionality and turbulence will occur at Reynolds numbers below Re = 200 (Coutanceau and Defaye [7]). Because of the two-dimensional nature of the current computations, turbulence and the effects of three-dimen-

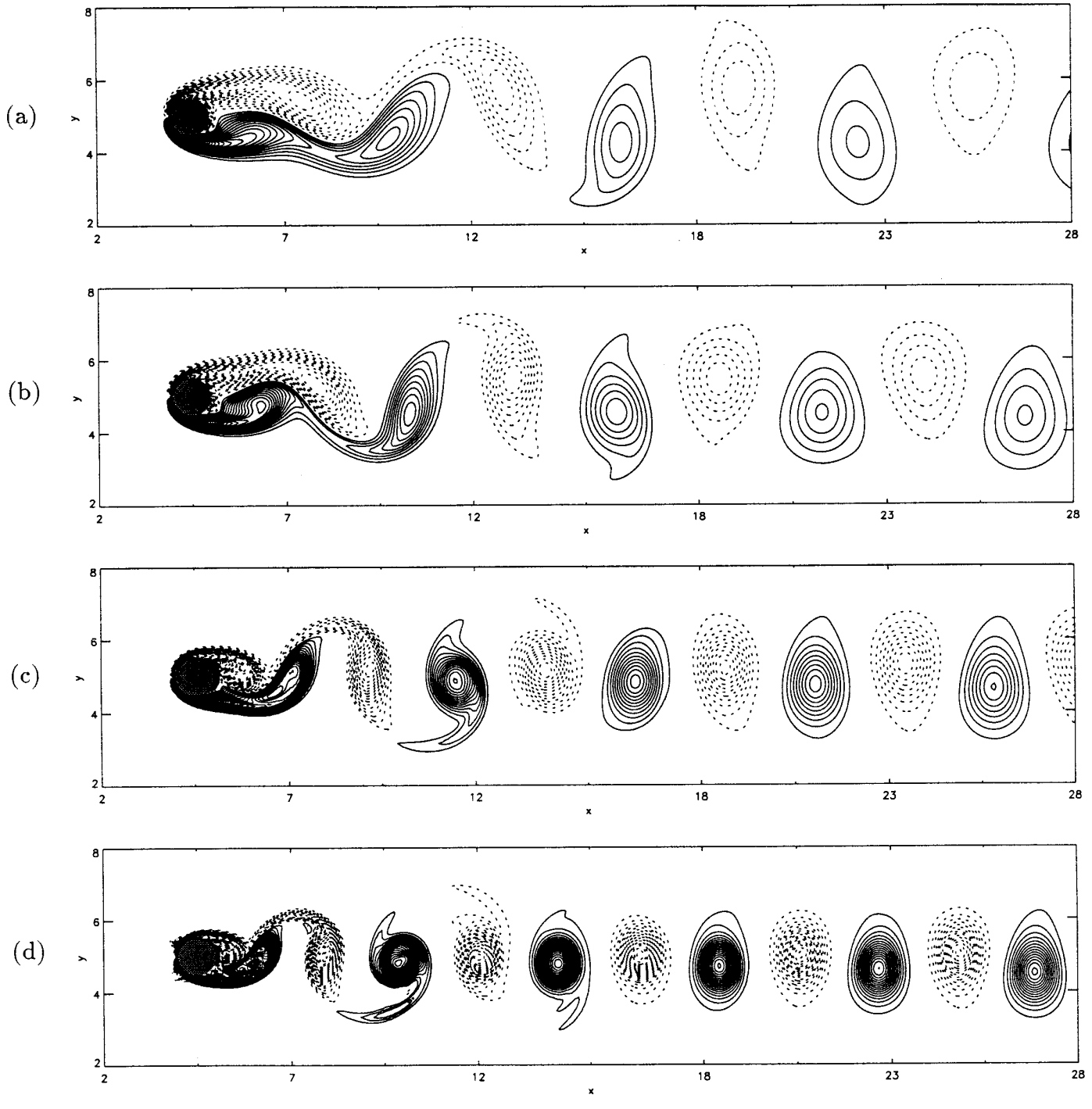

FIG. 9. Spanwise vorticity; dotted and solid lines denote negative and positive levels, respectively. (a) Re = 65; (b) Re = 100; (c) Re = 200; (d) Re = 400.

sionality cannot be obtained, however, the vortices shed from the cylinder at Re = 200 and 400 exhibit some irregularities associated with higher harmonics which subside as the vortices are convected downstream, forming a laminar Kármán vortex street (Figs. 9c–d).

Tables II and III summarize the drag coefficient (C_d), Strouhal number, the wave-length of the Kármán vortex street (λ), and the vortex speed (St λ) observed for the unsteady solutions and they provide comparisons with previous computational and experimental results. The Strou-

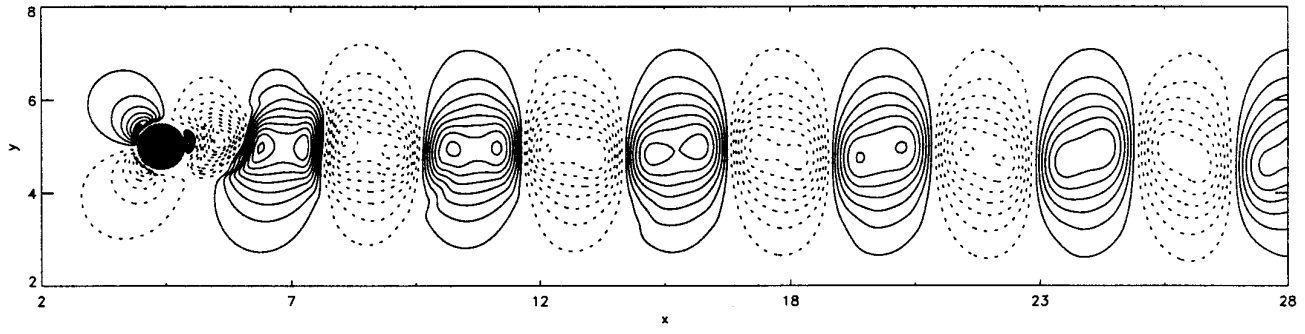

FIG. 10. Re = 400 : normal velocity, dotted and solid lines denote negative and positive levels, respectively.

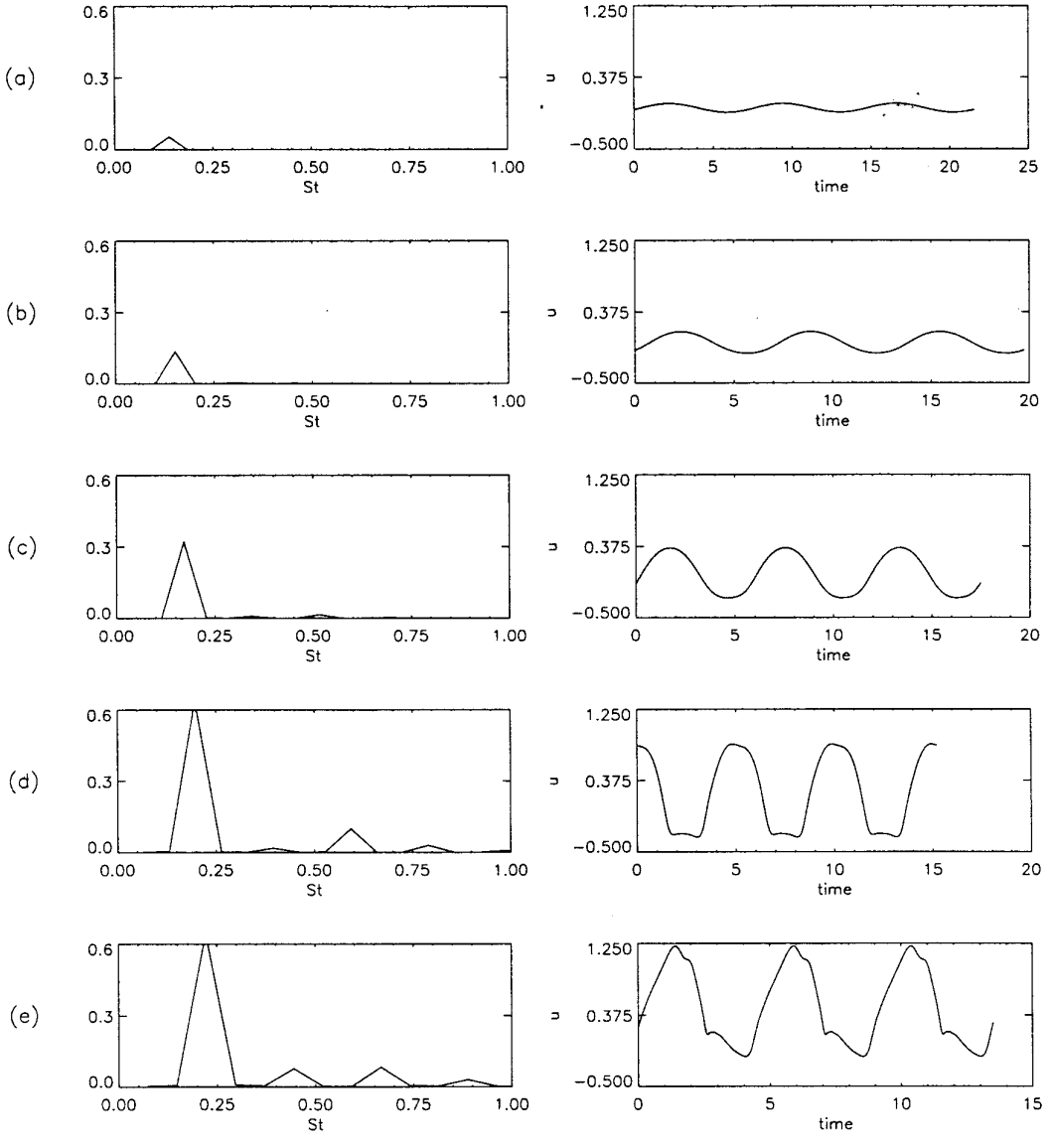

FIG. 11. Spectra and time signatures of streamwise velocity measured at $(x_d, y_d) = 0.9445, -0.325)$; x_d is the streamwise distance downstream from the cylinder and y_d is the normal distance from the symmetry axis of the cylinder. (a) Re = 50 (unsteady solution, Fig. 7); (b) Re = 65; (c) Re = 100; (d) Re = 200; (e) Re = 400.

TABLE III

Comparison of Quantitative Data with Previous Computational Results for Re = 100; Unsteady Flow Solutions

Re = 100	Present results	Gresho *et al.* [17]	Engelman & Jaminia [11]	Braza *et al.* [4]	Joran & Fromm [20]	Karniadakis *et al.* [21]
C_d	1.26	1.76	1.411	1.28	1.28	—
St	0.171	0.18	0.173	0.16	0.16	0.168
λ	5.5	5.2	5.32	—	—	—
St λ	0.94	0.93	0.915	—	—	—

hal numbers obtained from the present results are slightly higher than the experimental results; however, they correspond better than the values obtained by the majority of the other computational studies. The higher Strouhal number can be attributed to the size of the computational domain. Karniadakis and Triantafyllou [21] found that if the inflow boundary was too close to the cylinder or if the domain was not wide enough, a higher Strouhal number was obtained. The distance between the inflow boundary and the cylinder in the current study ($L_i = 4$) is comparable to the domain length used by Gresho *et al.* [17] and Engelman and Jaminia [11], but shorter than those used by Karniadakis and Triantafyllou [21], Braza *et al.* [4], and Jordan and Fromm [20]. Accordingly, as shown in Table III, the Strouhal number obtained in the current computations falls within the range of Strouhal numbers determined by the previous computational studies. We performed several test calculations with an expanded computational domain which revealed a slight drop in Strouhal number (from 0.171 to 0.168 for Re = 100) confirming that the proximity of the boundaries affects the vortex-shedding frequency.

In the present study the drag coefficient was calculated in a manner similar to Goldstein *et al.* [16]; the drag was found by considering the loss of fluid momentum in the domain, i.e.,

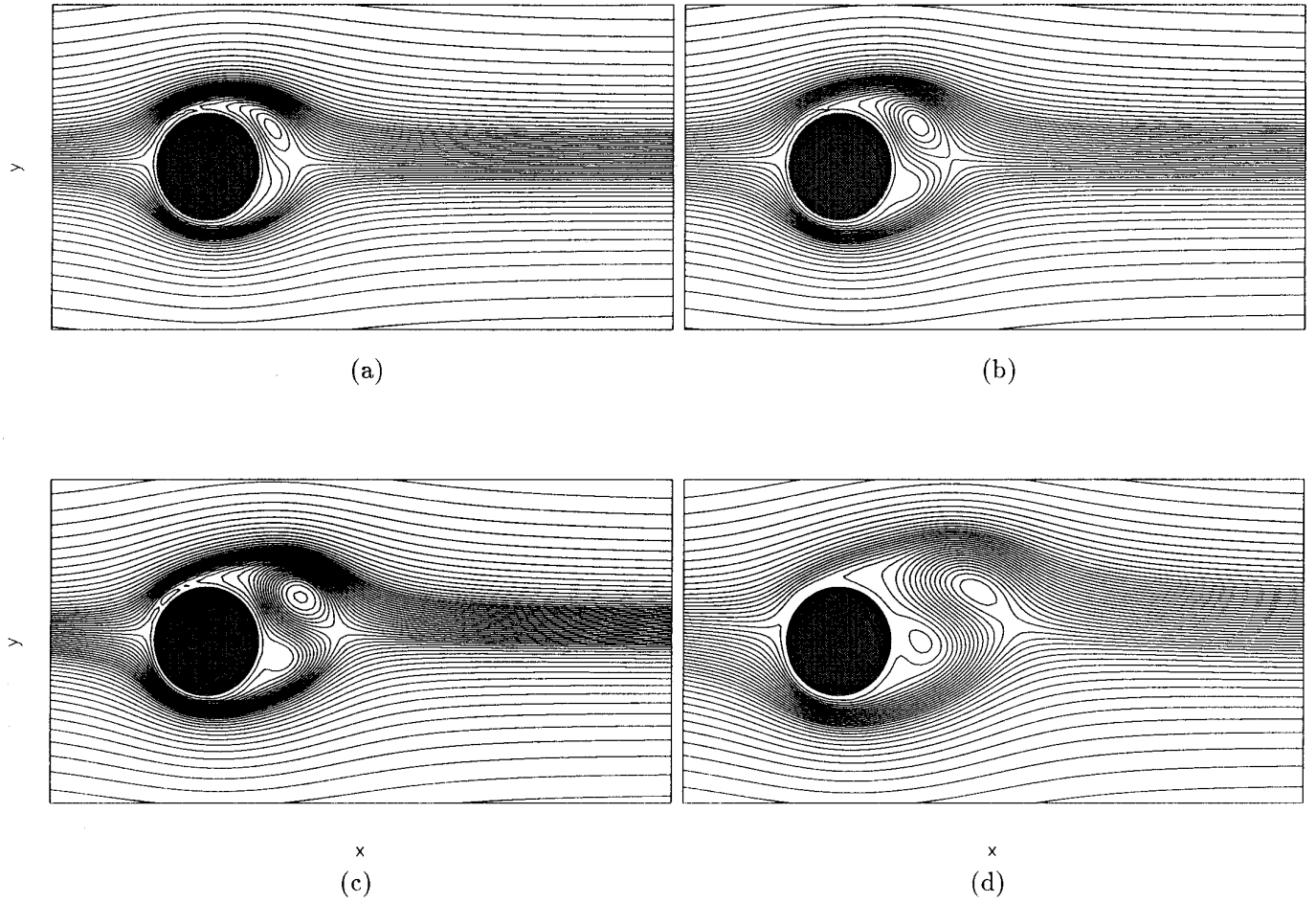

FIG. 12. Re = 200 : rotating cylinder. Time evolution of streamfunction contours. (a) $t = 1$; (b) $t = 1.5$; (c) $t = 2$; (d) $t = 3$; (e) $t = 4$; (f) $t = 5$; (g) $t = 5.5$; (h) $t = 6$.

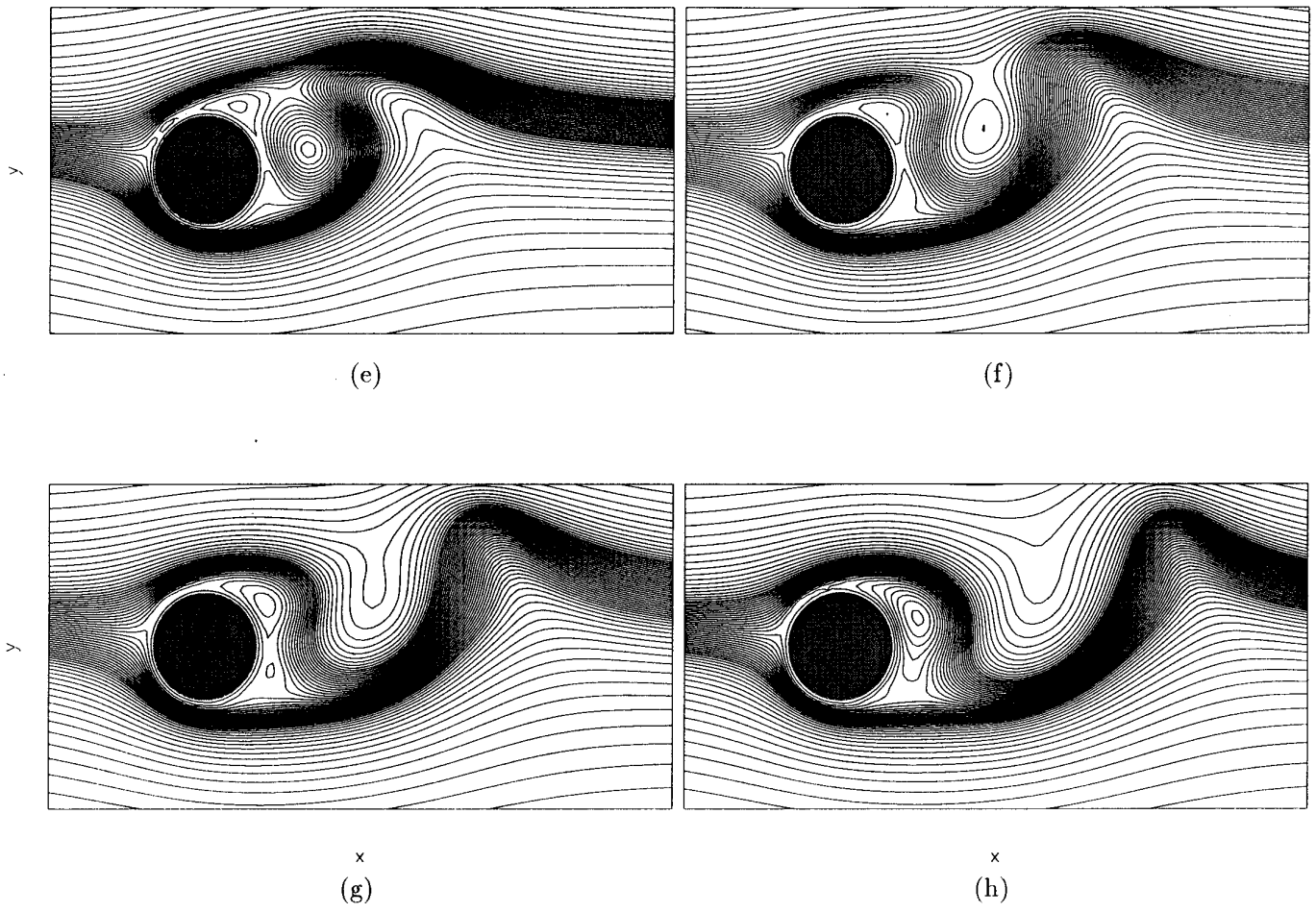

FIG. 12—*Continued*

$$C_d = 2 \int_{-\infty}^{\infty} \frac{U}{U_i} \left(1 - \frac{U}{U_i}\right) dy. \tag{8}$$

Due to the influence of the boundary conditions on the computation, U_i was defined as the maximum mean velocity measured at a distance $D/2$ upstream of the cylinder. As Tables II and III reveal, good agreement is found for values of C_d, in comparison with experiments and previous computational work.

Rotating Cylinder in Uniform Flow

The startup flow over a cylinder rotating counterclockwise in uniform flow was computed for Re = 200. The rotation rate of the cylinder was $\omega = 1$, resulting in a tangential velocity of one half the freestream velocity ($v_t = 0.5$). The motion of the cylinder was introduced by setting the components of $\mathbf{v}$ in Eq. (6) to the proper streamwise and normal velocities arising from the rotation of the cylinder, i.e., $\mathbf{v} = (-v_t \sin\theta, v_t \cos\theta)$, where θ is defined by the boundary points of the cylinder as $\theta = \tan^{-1}(y_b/x_b)$.

The characteristics of the startup flow at this Reynolds number and rotation rate consist of a primary eddy evolving at the top of the cylinder and a developing second eddy below the x-axis of symmetry (Figs. 12a–d). The second eddy moves upward (Figs. 12c–d) inducing two secondary vortices which merge to form a single vortex at time, $t = 6$ (Figs. 12e–h). The streamfunction contours obtained by the current study are in remarkable agreement with experimental observations (Coutanceau and Ménard [8]) and previous computational results (Badr and Dennis [1]). Figure 13 demonstrates excellent comparison between profiles of streamwise and normal velocity along the x-axis behind the cylinder obtained from the current computation and experimental measurements (Coutanceau and Ménard [8]).

Oscillating Cylinder in Uniform Flow

This computation was performed at Re = 200 with the cylinder oscillating parallel to the free-stream velocity at

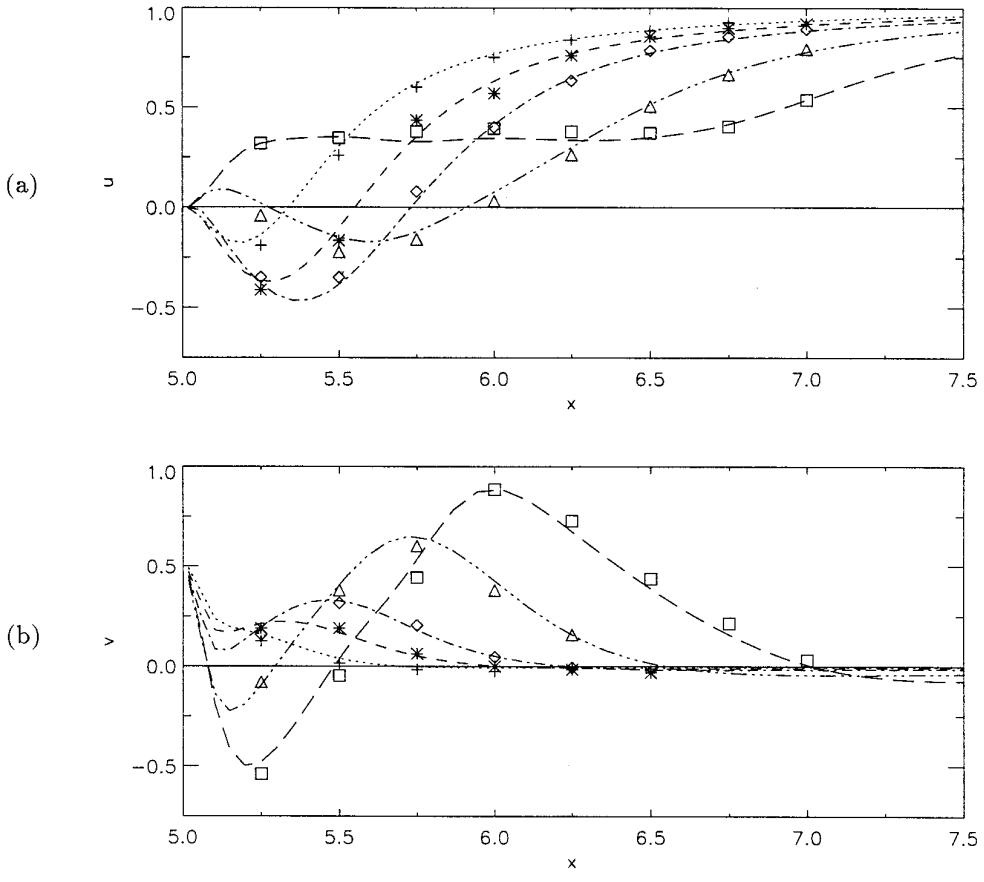

FIG. 13. Re = 200 : rotating cylinder. Time evolution of the velocity profiles along the x-axis of symmetry. (a) streamwise velocity; (b) normal velocity. Current computational results: ----------. $t = 1$; – – –, $t = 1.5$; – – – – –, $t = 2$; – – – – – – – –, $t = 3$; ——, $t = 4$. Experimental results [8]: +, $t = 1$; *, $t = 1.5$; ◇, $t = 2$; △, $t = 3$; □, $t = 4$.

a frequency, $f_c = 1.88$ St, i.e., 1.88 times the Strouhal frequency for the stationary cylinder. The amplitude of the oscillation resulted in a streamwise displacement of the cylinder of ± 0.24, and the cylinder motion was prescribed by setting the horizontal velocities on the boundary points to $u_b = A_c \cos(2\pi f_c t)$. The computations started with the cylinder stationary and oscillations were imposed once the solution reached a quasi-steady state.

For the parameters considered in the current study, the vortex shedding pattern of the stationary case at Re = 200 (Fig. 9c) is modified by the oscillation of the cylinder. This clearly depicted in the time evolution of spanwise vorticity contours over two oscillation periods of the cylinder (Fig. 14). During this time period an antisymmetrical mode A − III (Ongoren and Rockwell [22]) appears consisting of two clockwise vortices shed from the top of the cylinder and the evolution of a single counterclockwise eddy from the bottom. These vortices then form a vortex street with the weaker of the two clockwise vortices moving downstream alongside the counterclockwise eddy. These results are in excellent agreement with experimental observations (Griffin and Ramberg [18]; Ongoren and Rockwell [22]).

CONCLUSION

In this study, we applied a virtual boundary method to several steady/unsteady flow problems. The method models a no-slip boundary by an external forcing function added to the momentum equations. The computational results for both stationary and moving cylinders in uniform flow compare favorably with both experimental and previous computational studies and lend further evidence to the applicability of the virtual boundary technique for steady and unsteady flow problems. The oscillations caused by the virtual boundary method when used with a spectral discretization method were attenuated by the application of high-order finite differences.

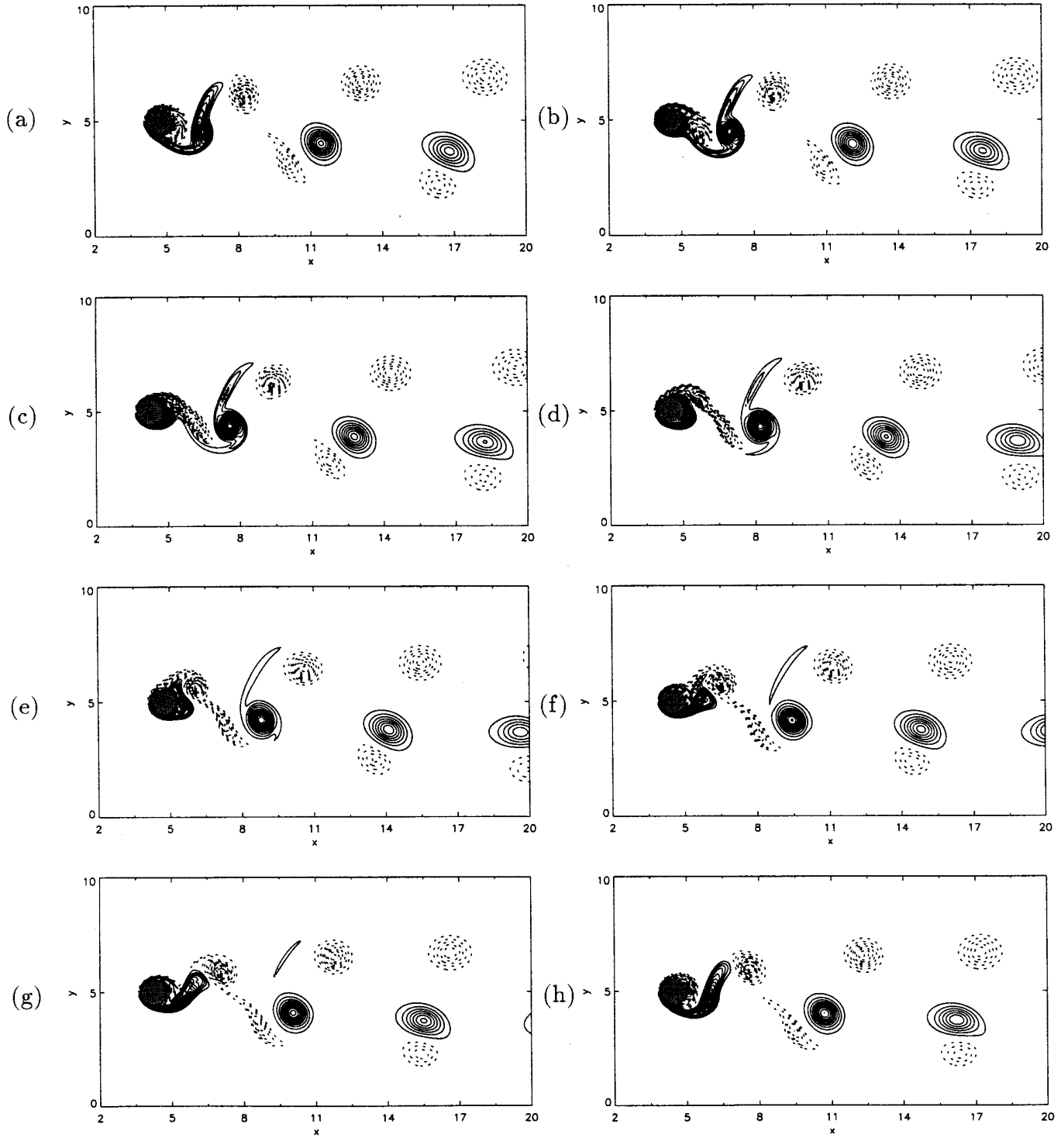

FIG. 14. Re = 200 : oscillating cylinder. Time evolution of spanwise vorticity contours; dotted and solid lines denote negative and positive contours, respectively. (a) $t = T/4$; (b) $t = T/2$; (c) $t = 3T/4$; (d) $t = T$; (e) $t = 5T/4$; (f) $t = 3T/2$; (g) $t = 7T/4$; (h) $t = 2T$ (T is the oscillation period of the cylinder).

ACKNOWLEDGMENTS

This work was supported by the Navy under Grant DOD N00014-94-1-0923. The authors thank James A. Fein for his continued interest in this work.

REFERENCES

1. H. M. Badr and S. C. R. Dennis, *J. Fluid Mech.* **158,** 447 (1985).
2. E. Berger and R. Wille, *Annu. Rev. Fluid Mech.* **4,** 313 (1972).
3. R. P. Beyer, *J. Comput. Phys.* **98,** 145 (1992).
4. M. Braza, P. Chassaing, and H. Ha Minh, *J. Fluid Mech.* **165,** 79 (1986).
5. R. Clift, J. R. Grace, and M. E. Weber, *Bubbles, Drops, and Particles* (Academic Press, New York, 1978), p. 154.
6. M. Coutanceau and R. Bouard, *J. Fluid Mech.* **79**(2), 231 (1977).
7. M. Coutanceau and J. R. Defaye, *Appl. Mech. Rev.* **44,** 255 (1991).
8. M. Coutanceau and C. Ménard, *J. Fluid Mech.* **158,** 399 (1985).
9. G. Danabasoglu, Ph.D. thesis, University of Colorado, 1992 (unpublished).
10. G. Danabasoglu, S. Biringen, and C. L. Streett, *Phys. Fluids A* **3,** 2138 (1991).
11. M. S. Engelman and M. Jaminia, *Int. J. Numer. Methods Fluids* **11,** 985 (1990).
12. A. L. Fogelson and C. S. Peskin, *J. Comput. Phys.* **79,** 50 (1988).
13. B. Fornberg, *J. Fluid Mech.* **98,** 819 (1980).
14. P. Freymuth, F. Finaish, and W. Bank, *Phys. Fluids* **29,** 1321 (1986).
15. D. Goldstein, T. Adachi, and H. Sakata, ''Modeling a Flow between Concentric Cylinders with an External Force Field,'' in *Proceedings, 11th AIAA Computational Fluid Dynamices Conference, Orlando, Florida, July 1993.*
16. D. Goldstein, R. Handler, and L. Sirovich, *J. Comput. Phys.* **105,** 354 (1993).
17. P. M. Gresho, R. Chan, C. Upson, and R. Lee, *Int. J. Numer. Methods Fluids* **4,** 619 (1984).
18. O. M. Griffin and S. E. Ramberg, *J. Fluid Mech.* **75**(2), 31 (1976).
19. A. Huser and S. Biringen, *Int. J. Numer. Methods Fluids* **14,** 1087 (1992).
20. S. K. Jordan and J. E. Fromm, *Phys. Fluids* **15,** 371 (1972).
21. G. E. Karniadakis and G. S. Triantafyllou, *J. Fluid Mech.* **238,** 1 (1992).
22. A. Ongoren and D. Rockwell, *J. Fluid Mech.* **191,** 225 (1988).
23. C. S. Peskin, *J. Comput. Phys.* **25,** 252 (1977).
24. C. S. Peskin, *Annu. Rev. Fluid Mech.* **14,** 235 (1982).
25. A. Roshko, NACA *Technical Note* 2913, 1953 (unpublished).
26. E. M. Saiki, S. Biringen, G. Danabasoglu, and C. L. Streett, *J. Fluid Mech.* **253,** 485 (1993).
27. E. M. Saiki and S. Biringen, ''Numerical Simulation of Particle Effects on Boundary Layer Flow,'' in *Transition, Turbulence, and Combustion, Volume I: Transition* edited by M. Y. Hussaini, T. B. Gatski, and T. L. Jackson (Kluwer Academic, Dordrecht, 1994, p. 267.
28. L. Sirovich, *Phys. Fluids* **10,** 24 (1967).
29. L. Sirovich, *Phys. Fluids* **11,** 1424 (1968).
30. C. L. Streett and M. Y. Hussaini, ICASE Report No. 86-59, 1986 (unpublished).
31. C. L. Streett and M. G. Macaraeg, *Appl. Numer. Math.* **6,** 123 (1989).
32. C. Tu and C. S. Peskin, *SIAM J. Sci. Stat. Comput.* **13,** 1361 (1992).